Gold Raspberry Shell Grown onto Nonspherical Lithium Niobate Nanoparticles for Second Harmonic Generation and Photothermal Applications

Rachael Taitt, Mathias Urbain, Kévin Bredillet, Zacharie Behel, Giacomo Ceccone, Jorge Bañuls-Ciscar, Sandrine Beauquis, Yannick Mugnier, Pierre-françois Brevet, Ronan Le Dantec, et al.

Particles II

Access the latest eBook →

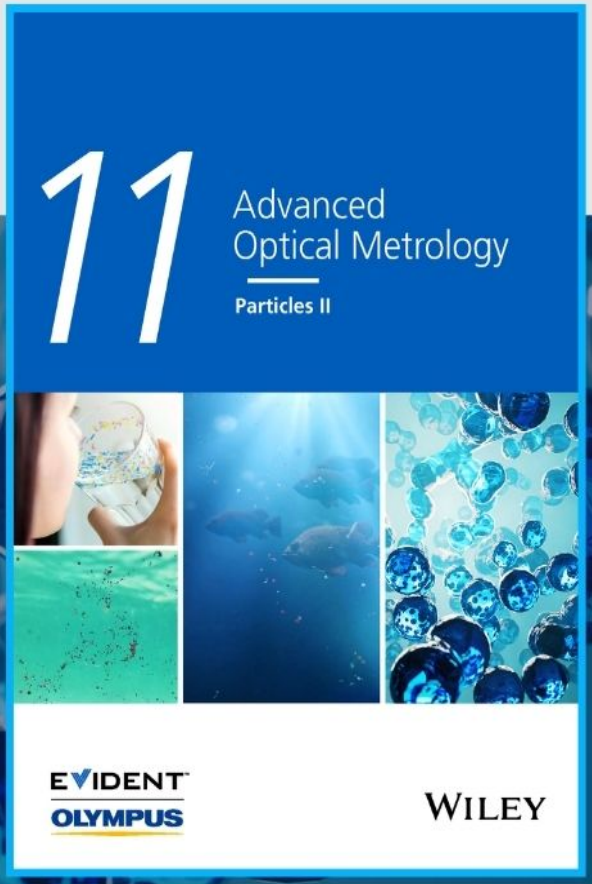

Impact on Biological Systems and the Environment

This eBook is dedicated to the research of Professor David Wertheim.
In collaboration with various groups, Professor Wertheim uses confocal microscopy to analyse the impact of different types of particles on human health and the environment, with a focus on human health-hazardous particles detected with solid-state nuclear track detectors (SSNTD). Download for free, today.

EVIDENT
OLYMPUS

WILEY

Gold raspberry shell grown onto non spherical lithium niobate nanoparticles for second harmonic generation and photothermal applications

*Rachael Taitt, Mathias Urbain, Kévin Brédillet, Zacharie Behel, Giacomo Ceccone, Jorge Banuls-Ciscar, Sandrine Beauquis, Yannick Mugnier, Pierre-François Brevet, Ronan Le Dantec, Yann Chevolot, and Virginie Monnier**

R. Taitt, V. Monnier

Univ Lyon, Ecole Centrale de Lyon, CNRS, INSA Lyon, Université Claude Bernard Lyon 1, CPE Lyon, INL, UMR5270, 69130 Ecully, France.

E-mail: virginie.monnier@ec-lyon.fr

M. Urbain, K. Brédillet, S. Beauquis, Y. Mugnier, R. Le Dantec
Université Savoie Mont Blanc, SYMME, F-74000 Annecy, France.

Z. Behel, P. F. Brevet

Université de Lyon, Université Claude Bernard Lyon 1, UMR CNRS 5306, Institut Lumière Matière, F-69622 Villeurbanne, France.

G. Ceccone, J. Banuls-Ciscar

European Commission, Joint Research Centre (JRC), 21027 Ispra, Italy.

This article has been accepted for publication and undergone full peer review but has not been through the copyediting, typesetting, pagination and proofreading process, which may lead to differences between this version and the Version of Record. Please cite this article as doi: 10.1002/ppsc.202200093.

Y. Chevolot

Univ Lyon, CNRS, INSA Lyon, Ecole Centrale de Lyon, Université Claude Bernard Lyon 1, CPE Lyon, INL, UMR5270, 69130 Ecully, France.

Keywords: plasmon, gold shell, lithium niobate nanoparticles, second harmonic generation, photothermia

Nanoparticles (NPs) containing a lithium niobate ($LiNbO_3$) core and a gold shell are prepared using a combination of seeded-growth and layer-by-layer approaches. The method includes first the surface charge reversal of lithium niobate with branched polyethyleimine, second, the electrostatic binding of gold seeds and third, successive reduction steps of gold chloride onto the gold-seeded $LiNbO_3$ NPs for the progressive and surface-directed growth of the gold shell. The influence of three synthesis parameters, namely pH, initial density of gold seeds covering the lithium niobate core and gold chloride concentration, on the NPs characteristics (structural properties, plasmon band, surface charge, hydrodynamic diameter) is studied. The progress of the gold shell growth is investigated by X-Ray photoelectron spectroscopy (XPS) and Time-of-flight secondary ion mass spectrometry (TOF-SIMS). In addition, we show that LN@Au core-shell NPs could emit a Second Harmonic Generation (SHG) signal when excited by a femtosecond laser. Finally, photothermal properties are studied, showing an increase of temperature of 8.6°C upon infrared excitation, with an estimated light-to-heat conversion efficiency of 40% and a specific absorption rate of 8000 W/g.

1. Introduction

Photothermal therapy (PTT) employs photothermal conversion agents (PTAs) to absorb light, and through their relaxation processes, release thermal energy to their local environment. Ideal PTAs should have a large absorption cross-section in any of the three biological windows (700-950 nm, 1000-1350 nm, 1550-1870 nm).[1] They should also have a high photothermal conversion efficiency (percentage of absorbed light converted to heat), good photothermal stability, be non-toxic and

allow for easy surface modifications.[2] The examples of PTAs found in the literature can be classified as noble metal-based NPs, semiconductor nanocrystals, carbon-based and organic semiconducting polymeric NPs.[3]

The noble metal PTAs, particularly the Au-based nanostructures are very attractive as Au has been extensively studied for its biocompatibility and ease of surface functionalization. Additionally, their shape and morphology also enable excitation wavelength tunability. The Au-based nanostructures that are interesting for PTT include nanorods, nanoshells and nanostars. Among them, the Au nanoshell structure is particularly appealing as it is inherently a hybrid NP combining another core material to provide multifunctional and multimodal applications (for example a gold shell encapsulating a material with contrast agent capabilities). Their light-to-heat conversion properties are due to their high absorption cross-section because of their localized surface plasmon resonances that can be tuned in a broad range of wavelength from 700 to 1000 nm depending on the shell thickness to core diameter ratio.[4,5] Recently, gold nanoshells grown onto silica cores were prepared and delivered intravenously to accumulate at the site of prostate tumours thanks to the enhanced permeability and retention (EPR) effect and these NPs are actually in phase 2 of a clinical trial for prostate cancer therapy.[6]

Gold nanoshells exhibiting a rough surface composed of closely-packed spherical gold NPs, also called nano-raspberries, are of great interest compared to smooth and continuous gold nanoshells. Indeed, the presence of 'hot spots' located in the gaps between gold NPs brings them specific functionalities finding applications for SERS enhancement and photocatalysis.[7] For PTT applications, advantage of these nanostructures is the possibility to tune their plasmon band over a large range of wavelengths covering the first and second biological windows. Furthermore, they are competitive with gold nanorods, nanostars and smooth nanoshells with similar specific absorption rates. Finally, their larger specific surface area compared to a spherical NP also allows to immobilize a greater number of biomolecules on their surface.[8]

The synthesis process of gold nanoshells onto silica NPs is based on a seeded-growth method[9,10] involving the adsorption of gold seeds onto the amine-modified silica surface followed by the growth of the gold shell using gold plating solutions containing chloroauric acid and potassium carbonate (K-

gold solution). With gold seeds acting as nucleation sites, reaction with a reducer produces Au atoms which then attach and cause the coalescing of the seeds. While the synthesis of gold nanoshells onto silica is well-developed, there are some challenges when transferring the same procedure to other core materials. First, it is due to the perfect spherical geometry and monodispersity of silica NPs, which may not be the case for other core materials. Another factor to consider is the silanization process, giving silica NPs a positive surface charge, which is highly sensitive to water. Therefore, silanization must be performed in non-aqueous environments in which it is difficult to maintain stable NP dispersions. In the literature, there are several examples of gold nanoshells grown on different cores such as $BaTiO_3$,[11] $KNbO_3$,[12] iron oxide[13,14] and other magnetic core,[15,16] silver NPs,[17] polystyrene,[18] and semiconductor.[19] Wang *et al*[11] synthesized a gold shell on 50-nm spherical $BaTiO_3$ NPs after hydroxylation of the surface with H_2O_2 and with 3-aminopropyltriethoxysilane to obtain amine terminations. In this case, the seed-mediated method was used to grow the gold shell with formaldehyde as a reducer. A homogenous core-shell structure was obtained with a gold shell thickness of approximately 10 nm and a maximum plasmon band at 800 nm. The synthesis of gold shell on iron oxide NPs has also been explored for biological applications. A layer-by-layer shell growth protocol was for instance designed by Lee *et al*.[14] Negatively-charged iron oxide particles, approximately 100 nm in diameter, were coated with a positive polymer, branched polyethylenimine (BPEI), causing a complete surface charge reversal evidenced by the zeta potential variation from negative to positive values. The polymer containing abundant amine groups facilitates the adsorption of separately synthesized gold seeds to the surface. Then an additional BPEI coating was performed followed by the reduction of $HAuCl_4$ in the presence of hydroxylamine hydrochloride. After repeating 6 times this last step, a gold shell of thickness 14.1 nm with a rough topography was obtained.

In this work, lithium niobate ($LiNbO_3$, LN) NPs were selected as a core material to grow a gold shell. Due to its non-centrosymmetric crystalline structure, $LiNbO_3$ is a mixed-metal oxide exhibiting piezoelectricity, electro-optics and efficient nonlinear optical properties at the nanoscale.[20] LN nanoparticles were recently used as exogenous labels for multiphoton imaging[21] and photo-triggering[22] approaches. Thus, coupled to a gold shell, these hybrid NPs may be used as multifunctional nanoprobes combining imaging and therapeutic properties.

Based on the Lee *et al* method, we report here a process to grow a raspberry-shaped gold shell with a plasmon band located in the near-infrared region, onto non-spherical $LiNbO_3$ NPs. In particular, we focused our study on the influence of several experimental parameters (pH, initial gold seed density and gold salt concentration) on the structure and plasmonic properties of the resulting hybrid NPs, with the objective to obtain homogeneous and stable colloidal NPs with a narrow size distribution. In addition, a detailed surface characterization procedure is provided at the different steps of the shell growth process. Finally, the Second Harmonic Generation (SHG) and photothermal properties of the optimized hybrid NPs aqueous dispersion are discussed.

2. Results and Discussion

The general protocol for the preparation of $LiNbO_3$ core – Au shell NPs (LN@Au) is depicted in **Scheme 1** and detailed afterwards.

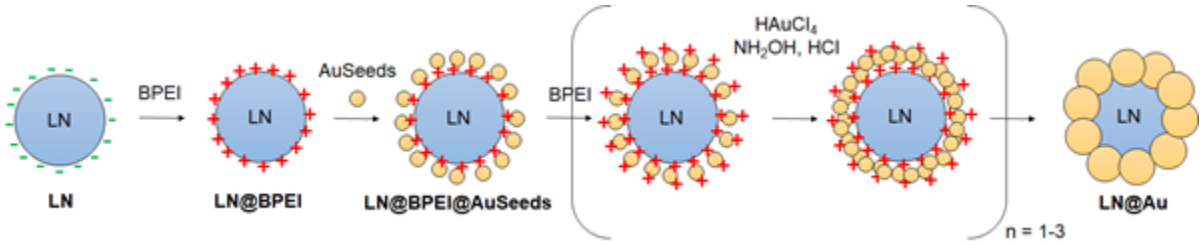

Scheme 1. Scheme of the protocol used for the layer-by-layer preparation of core-shell LN@Au NPs.

From the literature,[23] as well as from our experiments, the Au^{3+} reduction by NH_2OH, HCl to grow the gold shell is known to be catalyzed by the presence of AuSeeds on the core nanoparticles. The reduction reaction does not occur with only LN. Therefore our process is based on first the attachment of gold seeds on LN nanoparticles by electrostatic interaction thanks to BPEI. Please note that reduction does not also occur on LN@BPEI NPs without Au seeds. In the following, the nanoparticles and nanohybrids will be named after Scheme 1. Please note that for example LN@BPEI@AuSeeds3000 stands for the fact that a ratio of 3000 Au seeds per LN was used to synthesized the corresponding gold-seeded LN.

2.1. Preparation of Au-decorated $LiNbO_3$ nanoparticles (LN@BPEI@AuSeeds NPs)

Synthesis and characterizations of LN@BPEI@AuSeeds NPs were previously described.[24] Briefly, LN core NPs exhibit an average diameter of 34 ± 12 nm as determined by TEM and a hydrodynamic diameter of 135 ± 15.7 nm.[25] As shown in Figure S1 (Supporting Information), a pseudo-spherical shape was observed, with an average degree of sphericity of 0.8. The zeta potential of the LN dispersions was determined to be -43.2 ± 3.6 mV, leading to a high stability of the LN NPs dispersed in aqueous media. Gold seeds (AuSeeds) bear a negative surface charge of -25.3 ± 8.0 mV and a mean diameter of 2.5 ± 0.5 nm. Grafting of the AuSeeds onto the LN NPs can be based on electrostatic attraction. However, both LN NPs and AuSeeds were negatively charged. Therefore, LN NPs were modified with BPEI, a positively-charged polymer leading to LN@BPEI NPs with an average zeta potential of 36.0 ± 2.9 mV. The average hydrodynamic diameter by intensity of LN@BPEI was 159.6 ± 34.1 nm. Attachment of AuSeeds to the LN@BPEI NPs was then achieved by way of electrostatic and coordination interactions between the positive surface charge of LN@BPEI NPs and the negatively charged AuSeeds.

2.2. Layer-by-layer (LbL) preparation of LN@Au core-shell NPs (LN@Au NPs)

While there are examples of seeded-growth methods, involving iterative reductions of Au ions to produce core-shell nanoparticles, it often results in the uncontrolled and undesired encapsulation of multiple core particles within a single gold shell and thus in very polydisperse core-shell particles.[26] A layer-by-layer (LbL) process with alternate charge reversal was used here to manage the gold shell growth on the LN core as it is a versatile nanoscale synthesis technique to control the deposition of thin films.[27,28] A similar method for gold shell growth on spherical iron oxide NPs was proposed by Lee *et al*:[14] between each gold reduction step, a layer of the cationic polymer BPEI was used to completely coat the NPs. Starting from this protocol, we went further in the optimization process to investigate influences of the pH, initial gold seed density on the LN cores and $HAuCl_4$ concentration on the final NPs as discussed in the following sections.

2.2.1. Role of pH

In the protocol outlined by Lee *et al*,[14] the Au^{3+} reduction was performed under basic conditions, bringing the pH of the reaction medium to 11.5 before adding their gold-seeded iron oxide

nanoparticles to the aqueous solution. Although the pH at which the gold reduction is performed controls the particle growth of AuNPs[29] and thus the final gold shell morphology, this is balanced against the optimal pH for the protonation of the BPEI polymer (isoelectric point at around 11). It has to be noted that BPEI is 44% charged under neutral conditions,[30] with this percentage decreasing upon increasing pH. Therefore both basic (pH 11.5) and neutral (pH 7.7) conditions were tested here for the gold reduction reaction in the presence of LN@BPEI@AuSeeds NPs. At both pH conditions, a red-shifting of the UV-visible extinction profiles is observed (**Figure 1**a and Figures S2a-b, Supporting Information) upon the three successive reduction steps, labelled as R1, R2 and R3, respectively.

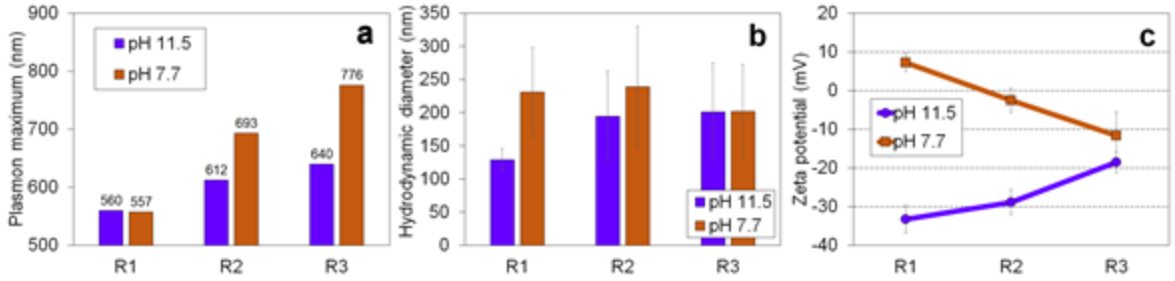

Figure 1. (a) Evolution of the plasmon band maximum wavelength (second peaks for R2 and R3), (b) hydrodynamic diameter and (c) zeta potential values after each reduction step for LN@Au NPs prepared with LN@BPEI@AuSeeds3000 as starting material at pH 11.5 and 7.7 and with [$HAuCl_4$] = 30 mM.

The progressive red-shifting of the plasmon band is thought to be due to the plasmon coupling interactions that occur between the initial gold seeds attached to the LN core. Indeed, at each reduction step, the interparticle distance between each gold seed decreases until coalescence. It red-shifts the longitudinal plasmonic resonance, until a complete shell is obtained. It has been shown that for interparticle distances shorter than 5 times the radius of the individual NPs, coupling effects become predominant, generally resulting in the red-shifting of the plasmon response.[31] Under pH 11.5 conditions, the extinction profiles at the different reduction steps evidenced single peak spectra (Figure S2a, Supporting Information). By R3, the extinction band spans from 500 to

1000 nm and has a maximum at 640 nm. Similarly reported by Lee *et al*,[14] after six reduction steps the UV-visible profile of their final NPs had a broad peak spanning from 500 to 1100 nm. The TEM images of the final LN@Au NPs prepared at pH 11.5 (Figure S3, Supporting Information) revealed that the gold deposition is quite heterogeneous among the primary LN@BPEI@AuSeeds NPs since some LN NPs were not completely coated with gold as evidenced by the EDS spectra (Figure S4a, Supporting Information). This may be indeed correlated to the lower degree of protonation of the amine groups of BPEI which is not promoting the electrostatic attachment of AuSeeds. This explanation is in agreement with the opposite evolution of the zeta potential values following the three successive reduction steps for LN@Au NPs prepared under pH 11.5 and pH 7.7 (Figure 1c). After R1, the positive charge of BPEI onto LN@Au NPs cannot be screened by negatively-charged AuSeeds at pH 7.7, while a negative surface charge is obtained at pH 11.5 suggesting that BPEI is quasi-neutral at this pH and that the negative charge is due to adsorption of AuSeeds or complexation to amine groups. Hydrodynamic diameters of LN@Au NPs synthesized under both pH were measured after R3 to be greater than 200 nm which is in agreement with the possible encapsulation of multiple LN cores in the Au coating (Figures S3 and S5, Supporting Information). Similarly, nearly identical standard deviations on the hydrodynamic diameters were obtained in these two pH conditions. For LN@Au NPs synthesized under pH 7.7, the extinction profile at R1 evidenced a single peak of maximum at 557 nm (Figure S2b, Supporting Information). This plasmon peak is attributed to individual, spherical gold NPs. However, after R2 and R3, a double peak appeared with the first maximum centered at 550 nm and a second one that is progressively red-shifted in the NIR region. At R3, the extinction profile had a narrower peak width as compared to that of the basic pH conditions, spanning from 700 to 900 nm, with the maximum centered at 776 nm. Corresponding TEM analysis revealed a smoother, spherical morphology of the Au NPs deposited on the LN surface (Figure S5, Supporting Information), giving the LN@Au NPs a raspberry-like morphology. This is in direct contrast to the spiky and rough surface morphologies reported by Lee *et al*.[14] Indeed, in seeded-growth methods, pH 7.7 tends to promote an even surface deposition of $AuCl(OH)_3^-$ (the predominant gold species at neutral pH), which upon subsequent reduction to Au^0 produces a more homogenous Au coating.[10] The TEM observation of these LN@Au NPs evidenced two size populations at 80-120 nm and above 200 nm corresponding very likely to both single and multiple LN core encapsulations (Figure S5, Supporting Information). Further EDS analysis of the

LN@Au NPs prepared under pH 7.7 revealed a co-localization of the Nb, O and Au elements thus confirming the core-shell structure. Distribution of these elements obtained from EDS chemical mapping is shown in **Figure 2** for a single LN@Au nanoparticle.

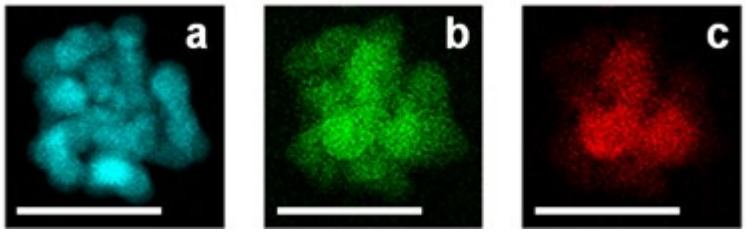

Figure 2. EDS chemical mapping of Au (a), O (b) and Nb (c) elements from a single LN@Au NP after R3. The synthesis conditions for the NP were LN@BPEI@Auseeds3000, pH 7.7, [$HAuCl_4$] = 30 mM. Scale bars correspond to 50 nm.

If gold deposition could be achieved on the LN@BPEI@AuSeeds NPs at two different pH conditions, a neutral pH was considered as more favorable for the following reasons: the narrower UV-visible band centered at 776 nm and the absence of uncoated LN cores. As such, the neutral pH conditions were selected as optimal with the aim to obtain a NIR-centered plasmon band.

2.2.2. Role of initial AuSeeds density on LN@BPEI

For a seeded-growth mechanism, the ratio between the gold seeds and the precursor of Au species to be reduced is a factor influencing the homogeneous or inhomogeneous growth of Au NPs.[32] In a previous study, we found from ICP-AES analysis that the maximum surface coverage of LN by AuSeeds at around 30% is already attained for both AuSeeds:LN ratios (1000 and 3000)[24] whereas XPS data revealed different Au:Nb atomic ratios at 0.91 and 1.28, respectively (Table S1, Supporting Information). Effect of these two AuSeeds densities on the final LN@Au structures and properties is thus worth to be studied. For both LN@BPEI@AuSeeds1000 and LN@BPEI@AuSeeds3000 samples, whose preparation is detailed in **Table 2**, initial zeta potential values below -30 mV are consistent with the necessary colloidal stability. The other synthesis parameters (pH 7.7 and concentration of $HAuCl_4$) were kept constant and are detailed in **Table 3**. After R3, a double peak is detected in the extinction profiles of samples prepared with 1000 and 3000 ratios (Figures S2c and S2b, Supporting

Information, respectively) while a single peak centered at 513 and 557 nm, respectively, is observed after R1 (**Figure 3**a). These two peaks that are attributed to the plasmon response of the non-interacting individual AuNPs on the LN surface, are still present after R2 and R3. The extinction maximum of the second peak at R2 was around 690 nm for both samples. After R3, a red-shift to 803 nm and 776 nm is monitored for LN@BPEI@AuSeeds1000 and LN@BPEI@AuSeeds3000, respectively. Whereas extinction profiles and measured hydrodynamic diameters (Figure 3b) lead to nearly identical results, variation of the zeta potential was quite different as shown in Figure 3c. Absolute values below 20 mV indicate a lower colloidal stability for LN@BPEI@AuSeeds3000 samples which are more prone to agglomeration whereas a continuous increase of the zeta potential till +30.2 mV is observed after each reduction step for LN@BPEI@AuSeeds1000 samples. This is also consistent with the larger size polydispersity derived for LN@Au NPs prepared with the highest initial AuSeeds density (Figure 3b).

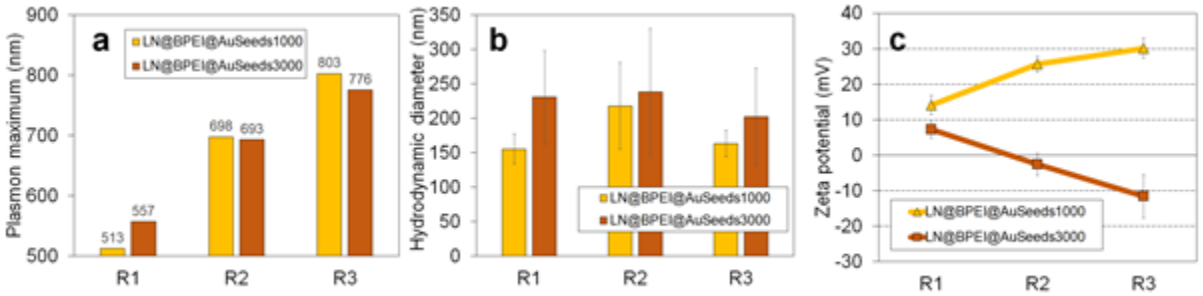

Figure 3. (a) Evolution of the plasmon band maximum wavelength (second peaks for R2 and R3), (b) hydrodynamic diameter and (c) zeta potential values after each reduction step for LN@Au NPs prepared with LN@BPEI@AuSeeds1000 and LN@BPEI@AuSeeds3000 as starting materials, at pH 7.7 and with $[HAuCl_4]$ = 30 mM.

Free Au NPs that are indeed evidenced by the TEM images (red circles in **Figure 4**f), may also contribute to the measured negative zeta potential (Figure 3c). Note that a larger Au:Nb ratio for LN@Au NPs prepared from LN@BPEI@AuSeeds3000 is also determined by XPS (**Figure 6b** and Table S1, Supporting Information). On the contrary, we did not observe any unattached Au NPs in the TEM images corresponding to the LN@BPEI@AuSeeds1000 samples (Figure S6, Supporting Information) , again in agreement with the lower size dispersions obtained after R3 in Figure 3b. A very similar gold

shell growth is observed though for both samples at each reduction step leading to the same raspberry-like morphology.

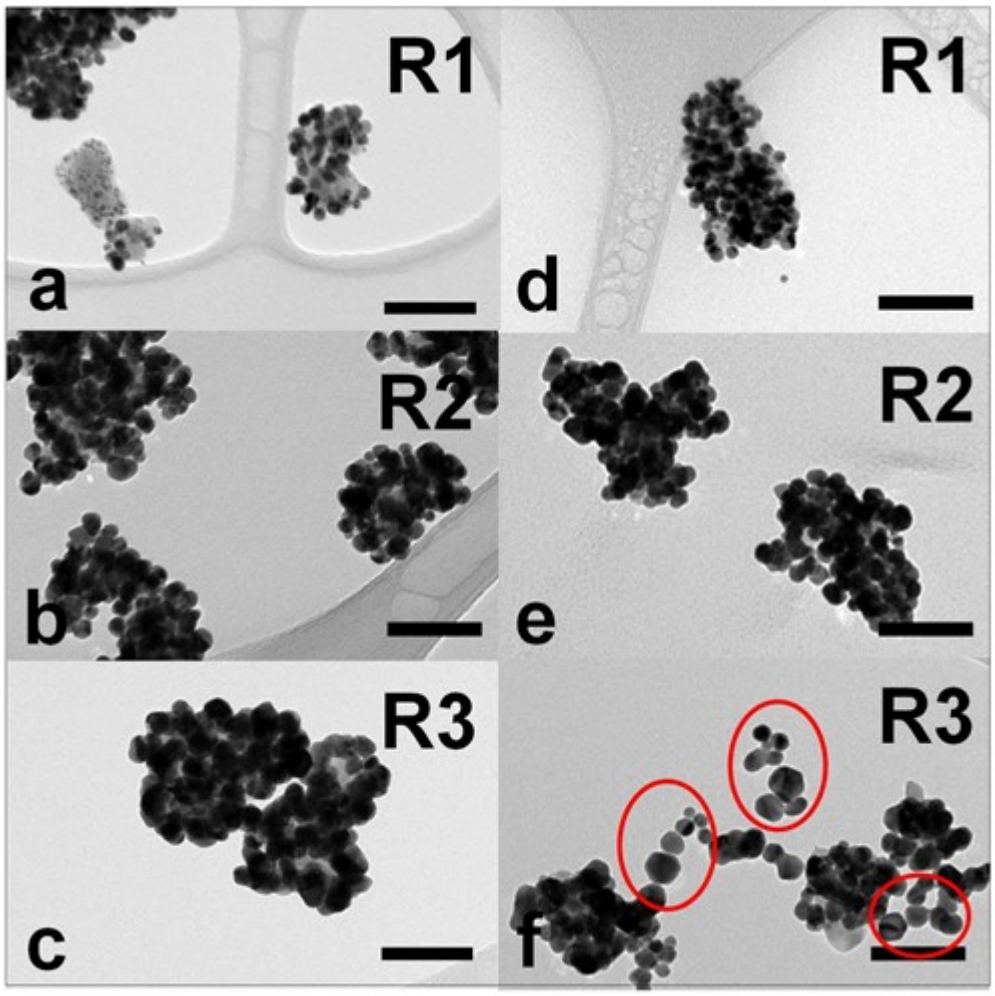

Figure 4. TEM images for LN@Au NPs prepared with LN@BPEI@AuSeeds1000 (a-c) and LN@BPEI@AuSeeds3000 (d-f) as starting materials, at pH 7.7 and with [$HAuCl_4$] = 30 mM. R1, R2 and R3 correspond to NPs obtained after the 1st, 2nd and 3rd reduction steps, respectively. Scale bars on TEM images correspond to 100 nm. Red circles indicate the presence of free Au NPs.

EDS analyses then demonstrate at R3 the detection of both Au and Nb or only Au on the outer surface of LN@Au NPs (Figure S7, Supporting Information). Interestingly, if free Au NPs are observed

in LN@Au samples prepared from LN@BPEI@AuSeeds3000, previous TEM investigations revealed the absence of unattached AuSeeds for every AuSeeds:LN ratio studied after their attachment to LN@BPEI.[24] Upon addition of NH_2OH, HCl to catalyze the reduction of Au^{3+} to Au^0, lack of space area between the closely-packed Au NPs at the surface of the LN@BPEI@AuSeeds3000 might explain the release of weakly bonded AuSeeds from the LN surface and their subsequent growth to produce unbound Au NPs. Due to the lower surface density coverage before reduction, this latter scenario is less prone to occur for the LN@BPEI@AuSeeds1000 samples that finally result in a more homogeneous population of LN@Au NPs.

2.2.3. Role of $HAuCl_4$ concentration

The gold salt concentration used at each reduction step was also investigated to get more insight of the gold reduction kinetics. In the work of Zhao *et al*,[33] the reaction kinetics in the gold-seeded growth of AuNPs was evaluated upon changing the reducer concentration resulting in a shell-morphology variation from smooth spheres to what they called 'nanoflowers', that are very similar to our raspberry-like structures, at increasing [reducer]/[$HAuCl_4$] ratios. Here, the NH_2OH, HCl reducer was always used in excess so that content of the limited reagent $HAuCl_4$ was varied around the default gold ion concentration of 30 mM used in previous works.[14,26] Three additional $HAuCl_4$ concentrations were tested, namely 3 mM, 10 mM and 100 mM, keeping the other optimized experimental parameters unchanged (Table 3). For [$HAuCl_4$] = 100 mM, R1 led to a rapid NPs agglomeration and formation of large aggregates that quickly settled to the bottom of the reaction vessel. Thus only the influence of the 3 mM, 10 mM and 30 mM $HAuCl_4$ concentrations will be discussed in the following. Contrary to the 30 mM concentration for which the extinction profile already exhibits a double peak after R2 (Figure S2c, Supporting Information), a continuous red-shifting of a single peak is found at each reduction for the 3 mM concentration (Figure S2e, Supporting Information). After R3, the final maximum extinction at 682 nm also demonstrates a blue-shift of 110 nm compared to the reduction at 30 mM of $HAuCl_4$ (**Figure 5**a).

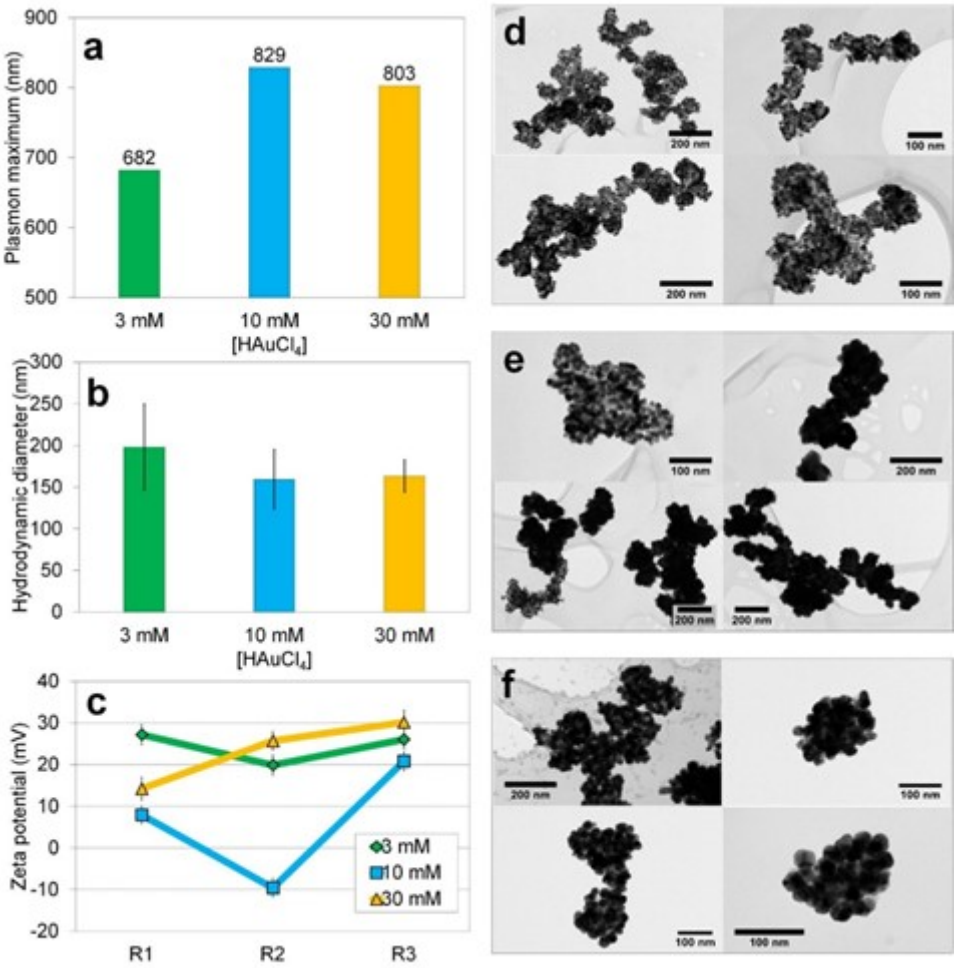

Figure 5. (a) Evolution of the plasmon band maximum wavelength obtained after R3 (second peak if two bands), (b) hydrodynamic diameter after R3 and (c) zeta potential values obtained after each reduction step for LN@Au NPs prepared with LN@BPEI@AuSeeds1000 at pH 7.7 and with [$HAuCl_4$] = 3 mM, [$HAuCl_4$] = 10 mM and [$HAuCl_4$] = 30 mM. TEM images of LN@Au NPs prepared with LN@BPEI@AuSeeds1000 at pH 7.7 with (d) [$HAuCl_4$] = 3 mM, (e) [$HAuCl_4$] = 10 mM and (f) [$HAuCl_4$] = 30 mM.

TEM imaging in Figures 5d-f is helpful to interpret the different extinction profiles since the LN surface at 3 mM of $HAuCl_4$ is not only partially covered but elongated Au NPs are also observed instead of the individual, almost spherical ones obtained with a 30 mM concentration.

Red-shifting of the single peak plasmon response at 3 mM of $HAuCl_4$ is thus attributed to the continuous growth of individual, non-interacting Au nanorods in agreement with the Gans theory for a fixed diameter of 5 nm and increasing aspect ratios.[34] Formation of metal nanorods by subsequent overgrowth has been intensively discussed and several growth mechanisms have been proposed to account for the subtle interplay between varying experimental parameters including the formation and deposition rates of Au^0, the presence of adsorbed species like surfactants and anions and, the surface energies of the three low-indexed facets, namely {001} or {110} and {111}.[34–37] Here at each reduction step, the zeta potential measured at 3 mM of $HAuCl_4$ is almost constant and ranged between 20 to 27 mV (Figure 5c) which is slightly below the initial value of 36.0 $\pm$ 2.9 mV when only BPEI is added to promote the surface charge reversal. A small amount of $AuCl(OH)_3^-$ ions is very likely preferentially adsorbed onto the high-energy {110} facets thus modifying the relative growth rates along the [001], [110] and [111] directions and promoting the anisotropic overgrowth. HRTEM images are supporting this hypothesis as the intereticular distance corresponding to (111) planes is the most frequently observed (Figure S8, Tables S2 and S3, Supporting Information).

At 30 mM of $HAuCl_4$, even though higher nucleation and deposition rates are expected, a continuous increase of zeta potential values is obtained from ~ 15 mV, after R1, till 30 mV after R3 (Figure 5c) evidencing a higher amount of adsorbed $AuCl(OH)_3^-$ ions at R1 onto the different facets of the primary AuSeeds. It thus results on similar deposition rates of Au^0 onto the {001} or {110} and {111} facets and a more isotropic overgrowth preserving the initial, almost spherical morphology of AuSeeds.

The extinction profile of LN@Au NPs produced using the 10 mM $HAuCl_4$ concentration is shown in Figure S2d (Supporting Information). After R1, the spectrum is similar to the ones obtained for the 3 mM and 30 mM concentrations, namely a single band, with a peak centered within the 530-550 nm range. Then at R2, a red-shifted band appeared at 690 nm, with a shoulder at 550 nm. Qualitatively this UV-visible spectrum is clearly different from the ones obtained at the same step for the 3 mM and 30 mM $HAuCl_4$ concentrations. Finally, at R3, a wide single band is observed, ranging from 550 to 1000 nm.

It can be concluded that the LN@Au dispersion produced using the 30 mM $HAuCl_4$ concentration exhibits a narrower plasmon response centered to around 800 nm in comparison to the other two concentrations. Interpretations are less straightforward for the LN@Au NPs prepared using the 10

mM $HAuCl_4$ concentrations since competing overgrowth mechanisms seemed to occur according to the measured large variations of the size (and size polydispersity) and zeta potential values at each reduction step as shown in Figures 5b and 5c, respectively. This was also evidenced from the TEM images provided in Figure 5e where partially covered LN cores with Au nanorods were again observed but unusual smooth shell morphologies were also detected corresponding to very large Au NPs. Note that the EDS analysis confirmed the presence of the Au and Nb elements in these nanostructures. As indicated above, evolution of the extinction profile after R1 and R2 (Figure S2d, Supporting Information) is thus different to the ones monitored for the concentrations of $HAuCl_4$ fixed at 3 mM and 30 mM. The last reduction performed here from the negatively-charged LN@Au NPs finally results in the broader and less defined extinction profile in agreement with the preparation of well-different shell morphologies.

To conclude about this systematic optimization of the synthesis parameters, **Table 1** summarizes the plasmon and colloidal properties of LN@Au NPs obtained under the different tested conditions.

Table 1. Summary of the plasmon and colloidal properties of LN@Au NPs obtained under the different synthesis conditions.

Starting LN@BPEI@AuSeeds	pH	$HAuCl_4$ [mM]	Plasmon maximum [nm][a)]	Hydrodynamic diameter [nm]	Zeta potential [mV]
LN@BPEI@AuSeeds3000	11.5	30	640	201.3 ± 73.5	-18.6 ± 2.7
LN@BPEI@AuSeeds3000	7.7	30	776	202.0 ± 70.5	-11.6 ± 6.1
LN@BPEI@AuSeeds1000	7.7	30	803	163.3 ± 19.3	+30.2 ± 2.8

LN@BPEI@AuSeeds1000	7.7	10	829	159.3 ± 35.8	+20.8 ± 2.3
LN@BPEI@AuSeeds1000	7.7	3	682	198.1 ± 51.5	+26.1 ± 2.2

[a)]Wavelength obtained for the maximum of the second band if two bands.

More stable and less aggregated LN@Au NPs with lower size dispersion were produced for LN@Au NPs prepared with LN@BPEI@AuSeeds1000 as starting material. However, at 3 mM of $HAuCl_4$ the plasmon response was not located in the near infrared region due to the non-interacting Au NPs covering the LN cores. Further reduction steps might be needed for the lowest concentration but at the detriment of the synthesis time. As observed on TEM images (Figure 5e), a concentration of 10 mM of $HAuCl_4$ lead to more heterogeneous LN@Au NPs with various morphologies. Therefore, because of the broad extinction profile with a maximum around 800 nm for the LN@Au NPs obtained at 30 mM of $HAuCl_4$, their low size dispersion and stability in aqueous media, the following parameters to consider for this LbL synthesis are: LN@BPEI@AuSeeds1000, neutral pH, 30 mM of $HAuCl_4$ reduced with 0.2 M NH_2OH, HCl after three gold reduction steps.

2.3. Progress of the gold shell growth during LbL–based synthesis

XPS and TOF-SIMS were used in a complementary fashion to provide further analysis on the surface of the NPs at different key steps in the LbL process. TOF-SIMS data mining was performed using principal component analysis (PCA).[38–40] Typical PCA outputs are Principal Components (PCs), loadings and scores. The scores describe the relationship between each PC and the samples, and the loadings describe a group of variables, peak intensities in our case, which define each PCs.[41,42] Figure S9a (Supporting Information) shows the scores for PC1 and PC2, whilst Figure S9b (Supporting Information) reports peaks intensities of most characteristic peaks related to PC1 and PC2 loadings. The score plot shows a clear separation between bare and functionalized LN NPs. In particular, PC1 is able to separate the LN bare NPs from the LN@Au and LN@BPEI@AuSeeds, whilst PC2 is able to further separate the BPEI-modified NPs from the LN@Au. Positive PC1 loadings (PC1+) show correlated peaks corresponding mainly to Li and Nb fragments whereas negative PC1 loadings (PC1-)

show correlated peaks corresponding mainly to fragments containing C, H, N and O. This suggests that PC1+ relates to the bare LN NPs and PC1- relates to BPEI. PC2+ shows gold fragments as the most intense peak areas, which suggests that this PC could represent mainly samples containing gold. Finally, the PC2- shows a C, H, N, O and Nb fragments as the most intense peak areas, representing both the LN NPs and BPEI. These results are in agreement with the surface chemistry expected for the different samples obtained during the LbL preparation of core-shell LN@Au NPs. In Figure S10 (Supporting Information), the XPS survey spectrum for LN NPs is given and compared to the XPS survey spectra of the LN@Au NPs at different steps of their synthesis starting from LN@BPEI@AuSeeds1000 and LN@BPEI@AuSeeds3000 NPs. A detailed indexation of the observed photoelectron peaks is also provided in Supporting Information. Figure 6a gives the atomic percentages obtained from XPS data.

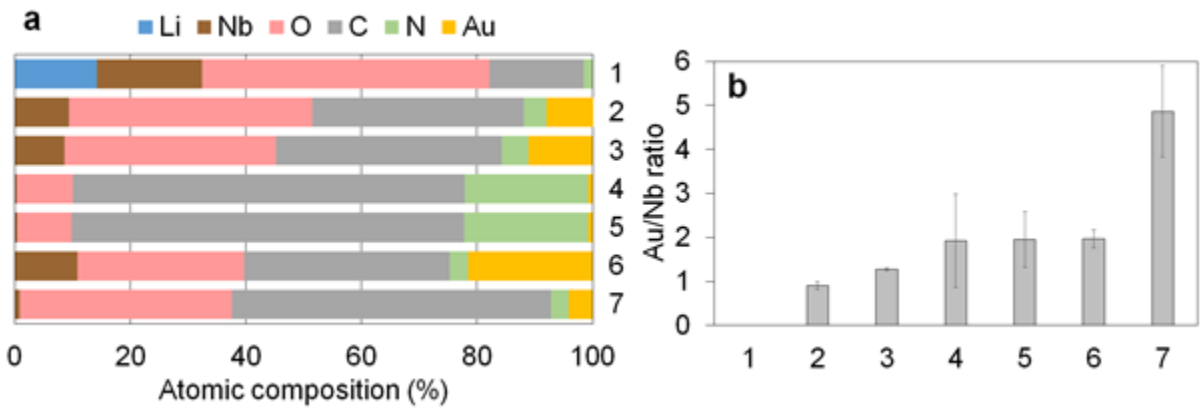

Figure 6. (a) Atomic composition (%) obtained by XPS for NPs prepared at the successive steps of the LbL process. Samples 1 to 7 correspond to (1) LN NPs, (2) LN@BPEI@AuSeeds1000, (3) LN@BPEI@AuSeeds3000, (4) LN@BPEI@AuSeeds1000@BPEI, (5) LN@BPEI@AuSeeds3000@BPEI, (6) LN@Au obtained from LN@BPEI@AuSeeds1000 after R3, (7) LN@Au obtained from LN@BPEI@AuSeeds3000 after R3, (b) Au to Nb ratio for samples 1 to 7.

Upon BPEI coating followed by gold-seeding of LN leading to LN@BPEI@AuSeeds1000, the presence of gold is observed and as expected, Nb and O atomic percentages decreased (Figure 6a, line 2). The Nb atomic percentage is reduced by almost a factor of 2 whereas the O atomic percentage is

reduced by a factor of 1.2. This discrepancy may be attributed to a higher contribution of the silicon substrate (SiO_2) on which NPs were deposited. C and N atomic percentages are increased due to the BPEI coating from 16.3 % to 36 % and from 1.5 % to 3.9 %, respectively. Similar trends are observed for LN@BPEI@AuSeeds3000 (Figure 6a, line 3). The Au atomic percentages are 8.5 % for LN@BPEI@AuSeeds1000 and 11.05 % for LN@BPEI@AuSeeds3000. As shown in Figure 6b, the increase of Au to Nb atomic ratio would suggest that the surface coverage is slightly increased when the AuSeeds to LN@BPEI ratio is increased from 1000 to 3000. For sample LN@BPEI@AuSeeds1000, TOF-SIMS PCA principle component 1 (PC1) scored negatively while its score was nearly 0 for LN@BPEI@AuSeeds3000 (Figure S9, Supporting Information). It suggests that the contribution of organic compounds containing N is higher for LN@BPEI@AuSeeds1000. The discrepancy with XPS results (C atomic percentage of 36.6 and 39.0 % for LN@BPEI@AuSeeds1000 and LN@BPEI@AuSeeds3000, respectively) may arise from the sampling depth of the two techniques: 1-3 nm for TOF-SIMS and 10 nm for XPS. LN@BPEI@AuSeeds1000 scores negatively for PC2 while LN@BPEI@AuSeeds3000 scores positively. Gold related ions contribute positively to PC2 and organic compound negatively. Therefore, TOF-SIMS results suggested that the amount of gold used for the synthesis of LN@BPEI@AuSeeds3000 was sufficient to reduce the signal coming from the BPEI.

Coating of LN@BPEI@AuSeeds1000 and LN@BPEI@AuSeeds3000 with BPEI, lead to a clear increase of C and N contributions while those of Au and Nb were drastically reduced (Figure 6a, lines 4 and 5). The C to N atomic ratio is above 3 while the theoretical C to N atomic ratio for BPEI is only 2 regarding its chemical formula (Figure S11, Supporting Information), suggesting some organic contamination. C1s core spectra (Figure S12, Supporting Information), only a low intensity contribution at 285 eV was observed suggesting a low hydrocarbon contamination. The N1s core spectra for both LN@BPEI@AuSeeds1000@BPEI and LN@BPEI@AuSeeds3000@BPEI (Figure S12, Supporting Information), show two contributions at 399 eV and 400 eV indicating that the amine function is partially protonated (1/3). Furthermore, both types of samples score in the negative PC1 and PC2 space showing a high contribution of organic compounds containing nitrogen ions as confirmed by the analysis of the loading plots (Figure S9b, Supporting Information).

The gold reduction steps, resulting in the formation of LN@Au core-shell NPs, are clearly observed by the increase of Au content while the atomic percentages of C and N are reduced (Figure 6a, lines 6 and 7). It must be noted that in the LN samples, a small N signal is also detected. If we are however

to attribute the entire N signal to presence of BPEI, the fact that nitrogen is still observed suggests that either the gold layer is thin enough to allow the N1s photoelectrons to escape or that the final gold layer is incomplete. This sample scores close to zero in PC1 which means that it is not rich in compounds containing Li, Nb and organic species containing N. This is however to be expected as the gold species from this gold surface layer will predominate resulting in the peak areas identified in TOF-SIMS. This is further confirmed by the positive score in PC2 which confirms that these samples are rich in gold. The inelastic mean free path of a nitrogen photoelectron (kinetic energy of approximately 1050 eV for an Al Kα source) through a gold layer is approximately 1.2 nm. Therefore, the XPS probing depth would be between 3-4 nm. The probing depth of TOF-SIMS is 1-2 nm. Consequently, if the layer was to be continuous, its thickness would rank between 1-4 nm. This was in agreement with the gold shell thickness derived from calculations using ICP-AES analysis determined to be 1.2 nm for LN@Au NPs prepared from LN@BPEI@AuSeeds, pH 7.7 and [$HAuCl_4$] = 30 mM (Supporting Information). From the TEM images of these optimized LN@Au NPs (Figures 4c and 5f) however, we measured Au NPs that comprised the gold shell with an average diameter of 26 ± 5.6 nm. With this diameter, an average number of 0.75 Au per LN core (see Supporting Information) was estimated, which is not in agreement with was is observed by TEM. Possible hypotheses for this inconsistency between what was observed by TEM and calculated from XPS and ICP-AES is that uncoated LN cores might still be present but not observed on TEM images. More probably, some LN@Au NPs are composed of multiple LN cores. Our calculations based on ICP-AES and XPS results supposed that there is only one LN core inside each LN@Au NP which leads to an underestimation of the gold amount inside the shell. Nevertheless, we supposed that LN@Au NPs with multi-cores of LN are only a minor part of the whole LN@Au population as the hydrodynamic diameter is only increased from 135 ± 15.7 nm for bare LN NPs to 163.3 ± 19.3 nm for optimized LN@Au NPs. Finally, concerning the Au to Nb atomic ratio (Figure 6b), it is significantly increased for LN@Au NPs compared to LN@BPEI@AuSeeds1000 and LN@BPEI@AuSeeds3000. The strongest increase observed for LN@Au NPs prepared from LN@BPEI@AuSeeds3000 can be attributed to the presence of free Au NPs (Figure 4f).

2.4. Second Harmonic Generation and photothermal properties of LN@Au core-shell nanoparticles

The emission spectra of the optimized LN@Au NPs suspension (pH 7.7, starting from LN@BPEI@AuSeeds1000 and after 3 reduction steps at 30 mM of $HAuCl_4$) were measured when

excited with a femtosecond laser at 800 nm, 1000 nm and 1200 nm (**Figure 7**). For each excitation wavelengths λ_{exc}, emission spectrum shows a dominant narrow SHG peak at $\lambda_{exc}/2$, superposed to a broad multiphoton luminescence background. This strong SHG signal could typically result from a favorable combination of the LN second-order nonlinear response and field enhancement due to the gold shell[43] but further studies are underway to establish the exact contribution of the gold shell.

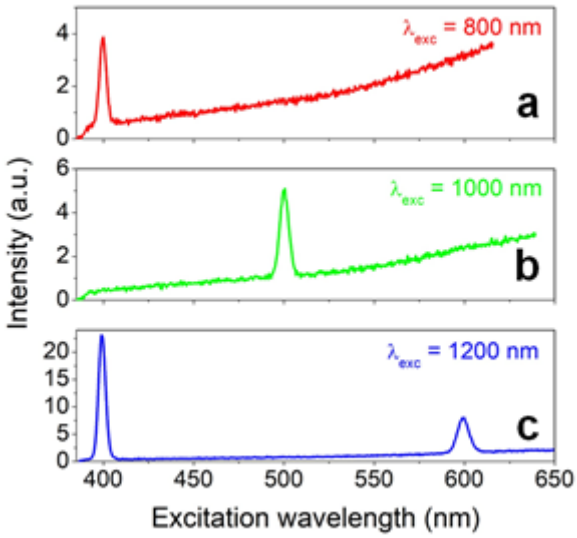

Figure 7. Emission spectra of the optimized LN@Au NPs dispersion obtained at excitation wavelengths of (a) 800 nm, (b) 1000 nm and (c) 1200 nm. Fundamental incident power was set to 50 mW. Each spectrum shows a dominant SHG peak and a Third Harmonic Generation signal is also detected for λ_{exc} = 1200 nm.

Photothermal evaluation of optimized LN@Au NPs was then achieved from thermographic imaging. ICP-AES measurements indicate that for a sample of 200 µL, the Au mass can be estimated at 34 × 10^{-4} mg. The temperature variation under continuous excitation at 808 nm is given in **Figure 8**a as a function of the irradiation time for several samples used as a control experiment. Note that only illumination of the LN@Au NPs results in a temperature increase as illustrated in the typical IR image of Figure 8b. After 34 minutes of irradiation, the temperature increase (δT) was recorded at 8.6°C.

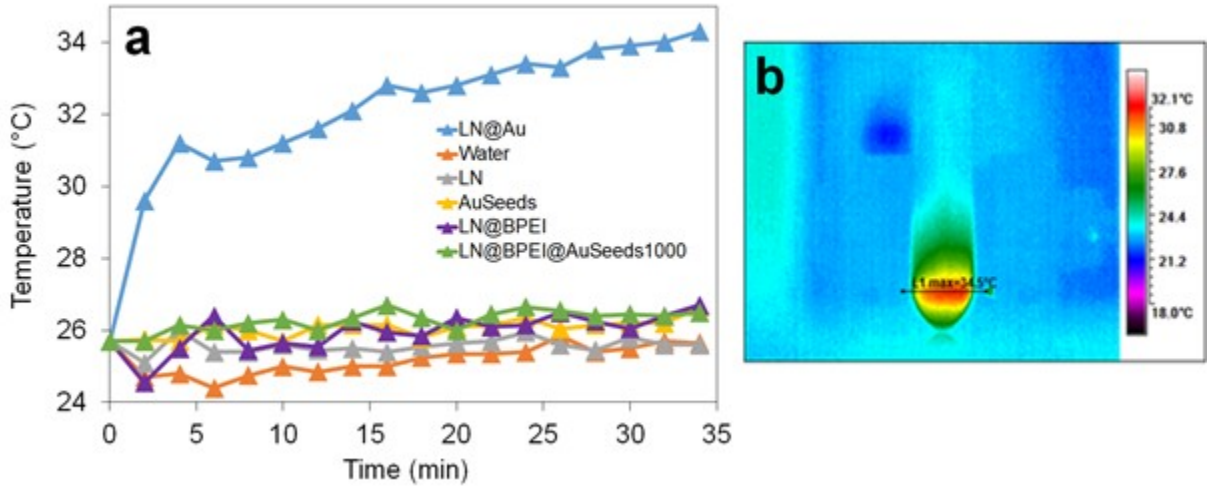

Figure 8. (a) Time-dependent temperature variations upon continuous illumination at 808 nm for several dispersions including LN@Au, LN, LN@BPEI@AuSeeds1000, LN@BPEI and AuSeeds. The temperature evolution of water alone was taken to normalize the curves. (b) Typical IR thermographic image of the heated LN@Au NPs dispersion.

To compare the LN@Au NPs to PTT agents found in literature, the light-to-heat conversion efficiency (η), was calculated using the equation from Jiang *et al*[44] (Supporting Information). The light-to-heat conversion efficiency of LN@Au NPs was here determined to be 40%. Using the same method for determining η, Plan Sangnier *et al*[8] reported a photothermal efficiency of 65% for their gold nano-raspberries*, i.e.,* AuNPs with a raspberry morphology. They also reported a conversion efficiency of 65% for gold nanorods and 35% for gold nanoshells, respectively.[45] In the work of authors Bi *et al*,[46] a record high photothermal conversion of 78.8% for gold nanostars is reported which was attributed to the optimization of the size of the core and the number of spikes to minimize the scattering contributions. This demonstrates the utility of a non-continuous gold shell for photothermal applications and the possibility to improve light-to-heat conversion efficiency by optimizing the geometry of the raspberry nanostructure. The Specific Absorption Rate (SAR) was evaluated to 8000 W/g, which is in the same order of magnitude than other gold nanostructures and several order of magnitude higher than magnetic NPs.[47]

3. Conclusion

In this paper, we discussed a seeded-growth synthesis method for the preparation of LN@Au NPs. The layer-by-layer process was proven to be suited to prepare raspberry-shaped core-shell LN@Au NPs. An optimization of the synthesis conditions (pH, initial AuSeeds density and gold concentration during the growth step) was conducted. We determined that starting with LN@BPEI@AuSeeds1000 NPs, and performing the gold reduction using 30 mM $HAuCl_4$ and 0.2 M NH_2OH, HCl in neutral (unaltered) pH, we obtained the optimal LN@Au NP dispersions in terms of stability, homogeneity of the gold shell and targeted plasmonic properties in the near-infrared region. Surface characterizations by XPS and TOF-SIMS determined the changing chemical environment of the NP surface at the different steps of the synthesis process. XPS was used to determine that the gold shell thickness was 1-4 nm. This was corroborated by the value obtained from ICP-AES analysis, giving a shell thickness of 1.2 nm. Second Harmonic properties of the non-centrosymmetric LN core were maintained after gold shell addition. The photothermal ability of the LN@Au NPs was demonstrated and a light-to-heat conversion efficiency of 40% was determined. Therefore, these LN@Au core-shell NPs offer dual capabilities for multiphoton imaging (with scattering of second and third harmonic signals) and for photothermal therapy and could be thus considered as potential theranostic nanoprobes.

4. Experimental Section

4.1. Materials

Lithium niobium ethoxide ($LiNb(OEt)_6$), (99+% metal basis, 5% w/v in ethanol) was obtained from Alfa Aesar, Teflon cup model number 4749 was obtained from Parr Instrument, and Nalgene centrifugation tubes were obtained from ThermoFisher. Butane-1,4-diol (99%), ethanol, sodium hydroxide (NaOH) pellets, tetrakis(hydroxymethyl)phosphonium chloride (THPC) solution (80% w/v in water), polyethylenimine branched (BPEI), ~25000 g/mol, gold (III) chloride trihydrate ($HAuCl_4$, $3H_2O$, ≥99.9%, trace metal basis), NH_2OH, HCl (hydroxylamine hydrochloride) were all obtained from Sigma Aldrich. The $HAuCl_4$, $3H_2O$ was dissolved in water to give a concentration of 313 mM, stored in

a dark bottle and kept in the dark until needed. Unless otherwise stated, water (18.2 MΩ.cm) was used.

4.2. Synthesis of $LiNbO_3$ nanoparticles (LN NPs)

As already described,[25] LN NPs were synthesized by a non-aqueous solvothermal alkoxide process. Inside an autoclave equipped with a 23 mL Teflon cup, 2.25 mL of lithium niobium ethoxide and 1.25 mL of butane-1,4-diol were added. The mixture was then heated in an oven (Memmert, Schwabach, Germany) increasing the temperature by 5°C intervals every ten minutes until the temperature of 230°C was attained, and this temperature was maintained for three days. After cooling to room temperature, the precipitate was transferred to Nalgene centrifuge tubes. Three centrifugation rounds at 13500 rpm for three minutes were carried out to collect the powder which was washed in ethanol under sonication for ten minutes. The final LN NPs were dried at 75°C. They were then dispersed in water at a mass concentration of 1 g/L.

4.3. Synthesis of LN@Au core-shell NPs

4.3.1. Polymer adsorption onto LN NPs

BPEI polymer was used to coat the LN NPs. Firstly, 5 mg of BPEI was weighed into a glass reactor vessel and dissolved in 5 mL of water while heating at 90°C. The temperature was maintained at 90°C with continuous stirring and 0.5 mL of the 1 g/L LN NP dispersion was added to the reactor and left for 4 h. The mixture was allowed to cool to room temperature and then the resulting BPEI coated LN NPs (LN@BPEI NPs) were separated from any BPEI in excess by performing six, 10-minute centrifugation washing steps in water at 10°C and 9100 g. These six centrifugation runs were found to be necessary to avoid the presence of free BPEI leading to the further growth of free Au NPs. The LN@BPEI NPs were then re-dispersed in water to give a final concentration of 0.35 g/L.

4.3.2. Preparation of Au-decorated LN NPs (LN@BPEI@AuSeeds NPs)

The preparation of LN@BPEI@AuSeeds NPs was achieved in a two-step process as detailed previously.[24] Firstly, gold seeds (AuSeeds) were synthesized using the protocol reported by Duff *et al*.[48] In brief, 540 µL of 0.1 M NaOH was added to 45.5 µL of water followed by 2.14 µL of a 4.2 mM solution of THPC. While stirring, 360 µL of 25 mM $HAuCl_4.3H_2O$ solution was added to the mixture and the stirring was continued for ten minutes, with the mixture undergoing a color change from colorless to brown-red within less than 30 seconds. The AuSeeds dispersion was stored at 4°C and used for further procedures up to two months post synthesis. To attach the AuSeeds onto LN@BPEI NPs, the following theoretical ratios of AuSeeds to LN NPs (in number) were used: 1000:1 and 3000:1, using the volume of reactants presented in Table 2. The final volume was 10.588 mL in each case.

Table 2. Volumes and final concentrations of the AuSeeds dispersions used for varying the density of AuSeeds attached to the LN@BPEI surface. The stock AuSeed dispersion had a concentration of 2.32×10^{14} NPs/mL. For each sample, 1 mL of 1.58×10^{12} NPs/mL of LN@BPEI was used.

Sample Name	Volume of AuSeeds dispersion [mL]	Volume of H_2O [mL]	Final AuSeeds concentration [NPs/mL]	Theoretical AuSeeds: LN ratio
LN@BPEI@AuSeeds1000	3.486	7.102	6.97×10^{13}	1000
LN@BPEI@AuSeeds3000	10.459	0.129	2.09×10^{14}	3000

Then, while under stirring, 1 mL of LN@BPEI NPs (0.35 g/L or 1.58×10^{12} NPs/mL) was added to the AuSeeds dispersions and allowed to mix for 30 minutes. After keeping the NP dispersion for 24 hours at 4°C, two 10-minute rounds of centrifugation at 10°C and 9100g were carried out to remove the

unattached AuSeeds in the supernatant. The resulting LN@BPEI@AuSeeds NPs were redispersed in 1 mL of water to obtain again a final concentration of 0.35 g/L.

4.3.3. Layer-by-layer preparation of LN@Au core-shell NPs.

BPEI, 4 mg, was weighed in a reaction vessel and dissolved in 5 mL of water at 60°C. Upon complete BPEI dissolution, 1 mL of 0.35 g/L LN@BPEI@AuSeeds was added and left to mix for two hours while maintaining the temperature at 60°C. The NP dispersion was cooled to room temperature, and transferred to a centrifuge tube, where two centrifugation rounds of 10 minutes at 10°C and 9100g were conducted, removing the supernatant and replacing it with water between each centrifugation. The NPs were then re-dispersed in 1 mL of water. In a 50 mL Nalgene tube, 18 mL of water was added. Depending on the experiment, the pH of the dispersion was either kept at approximately 7.7 or adjusted at 11.5 using 0.1 M NaOH. Then, while under stirring, 1 mL of the LN@BPEI@AuSeeds@BPEI dispersion was added to the 18 mL of water and allowed to homogenize for one minute, 50 µL of $HAuCl_4$ solution was then added and, finally, 75 µL of 0.2 M NH_2OH, HCl. The contents of the Nalgene tube was left under stirring for 10 minutes after which two centrifugation rounds of 10 minutes at 10°C and 9100g were performed, removing the supernatant and replacing it roughly by 5 mL of water between each centrifugation. The final NPs were again dispersed in 1 mL of water. This entire procedure was then repeated two more times. During the growth process, the critical step was to remove the main part of the supernatant without taking out the precipitate. Indeed, removing some part of the precipitate would lead to a change in NPs concentration while keeping supernatant would cause the growth of free Au NPs. For this purpose, thin capillary pipette tips were used to remove the last part of the supernatant directly in contact with the precipate. The above protocol was modified to examine the influence of pH, initial gold seed coverage, and $HAuCl_4$ concentration on the final hybrid NPs. The investigated experimental parameters are detailed in Table 3.

Table 3. Experimental conditions for the layer-by-layer gold shell growth.

Parameters	Samples

pH	1) LN@BPEI@AuSeeds3000**, pH 11.5**, [$HAuCl_4$] = 30 mM 2) LN@BPEI@AuSeeds3000, **pH 7.7**, [$HAuCl_4$] = 30 mM
LN@BPEI@AuSeeds	1) **LN@BPEI@AuSeeds1000**, pH 7.7, [$HAuCl_4$] = 30 mM 2) **LN@BPEI@AuSeeds3000**, pH 7.7, [$HAuCl_4$] = 30 mM
[$HAuCl_4$]	1) LN@BPEI@AuSeeds1000, pH 7.7, **[$HAuCl_4$] = 3 mM** 2) LN@BPEI@AuSeeds1000, pH 7,7, **[$HAuCl_4$] = 10 mM** 3) LN@BPEI@AuSeeds1000, pH 7.7, **[$HAuCl_4$] = 30 mM** 4) LN@BPEI@AuSeeds1000, pH 7.7, **[$HAuCl_4$] = 100 mM**

4.4. X-Ray Photoelectron Spectroscopy (XPS)

XPS measurements were performed with an Axis Ultra-DLD from Kratos. A monochromatic X-ray source Al Kα = 1486.6 eV, was operated at a power of 225 W. Wide scan spectra were recorded from 0 to 1200 eV binding energy in hybrid mode, "slot" (400 x 700 μm^2 analysis area) and FoV2 (100 µm spot) at 160 eV and 80 eV pass energy, respectively, whereas core level spectra were recorded in 'hybrid' mode using pass energy of 40 eV. The take-off angle respect to the sample normal was 0° for survey and high-resolution (HR) spectra for an operating pressure at 1.5×10^{-8} mbar. Surface charging was compensated using low energy (3.8 eV) electrons and adjusted using the charge balance plate on the instrument. All the spectra were processed with CasaXPS (V2.3.22). Spectra were calibrated setting hydrocarbon C1s at 284.6 eV and Au $4f_{5/2}$ at 84.00 eV. The surface composition was evaluated from the survey spectra, after background subtraction, using Relative Sensitivity Factors (RSF) based on Scofield cross sections and corrected for magic angle emission,

electron mean free path and spectrometer's transmission functions. Peak fitting was performed with no preliminary smoothing. Lorentzian finite functions, LF(a,b,w,n), were used to approximate the line shapes of the fitting components after a Tougaard U3 background subtraction.

4.5. Time-Of-Flight Secondary Ion Mass Spectrometry (TOF-SIMS)

TOF-SIMS (ToF IV, ION TOF GmbH, Germany) was also employed to characterize samples chemistry. The accelerating voltage of the liquid metal ion gun (LMIG) was 25 keV, Bi_3^{++} was employed as source of primary ions rastering over an area of 200 x 200 μm^2. The analyses were carried out in static conditions keeping the ion dose below 10^{12} ions/cm^2. Acquisition time was 45 s, with a beam current of 0.5 pA and primary ion beam in pulsed mode. The sample was deposited on a clean silica substrate and a low-energy electron flood gun was used for charge compensation during analysis. Eight spectra were acquired for each sample in positive and negative polarity. TOF-SIMS data were pre-processed using the SurfaceLab V6 software (IONTOF GmbH). Mass spectra were calibrated using unique mass calibration peak lists containing C^+, CH_2^+, CH_3^+, $C_3H_5^+$, $C_6H_3^+$, $C_6H_7^+$, $C_8H_9^+$ for the positive polarity, and C^-, CH^-, CH_2^-, C_2H^-, C_3H^-, CHO_2^-, $C_4H_3^-$ for the negative polarity spectra. After a preliminary inspection of the data, and considering the high yield of certain fragments in the positive spectra coming from irrelevant chemistry (or contaminants), further analysis was only carried out with the negative polarity spectra. A list containing a combination of peak areas of characteristic peaks from each type of sample was created and exported as a text file excluding saturated peaks. The text file was uploaded into the simsMVA software (http://mvatools.com) for Principle Component Analysis (PCA). Data was normalized by total ion intensity, Poisson scaled and mean centered before performing PCA.

4.6. Second Harmonic Spectroscopy (SHS)

SHS experiments were performed with an experimental set-up already presented in a previous work.[49] Briefly, a tunable femtosecond laser (680 to 1300 nm, Insight X3 Spectra-Physics) is used as the excitation source and focused through an achromatic lens (f = 30 mm) into a cuvette containing the nanoparticle suspension. The emitted signal is collected perpendicular tot he incident laser and analyzed by a spectrometer (Andor Shamrock 193) coupled to a CCD camera (Andor iDus 401). A

low-pass filter (Thorlabs FESH700) is placed in front of the spectrometer entrance to remove unwanted light scattered from the fundamental beam.

4.7. Photothermal measurements of NPs dispersions

A home-made laser set-up (Figure S13, Supporting Information) was configured for conducting the photothermal evaluation of the NP dispersions. In brief, a sample holder was fixed inside a black box. A F110SMA-780 lens from Thorlabs was attached to an 808 nm continuous wave (CW) laser, with a beam spot size of 1.36 mm by way of a fiber optic cable. The measured output power was 47 mW/cm^2. The laser was then positioned at 0° with respect to the normal of the liquid surface. An IR-thermographic camera (THERMOPRO TPS8S) was positioned at 90° with respect to the laser beam, at a distance of 10 cm from the sample. For each experiment, 200 µL of the sample was placed in a 2 mL microtube. The IR-thermographic camera was used to capture images of the microtube in real time. An image was taken before switching on the laser to have the reference temperature for the tube and its content. Then the laser was switched on and the IR images containing the temperature data were taken at one-minute intervals for 30 minutes. The temperature vs time profiles for each sample are then obtained from the image analyses provided by the Guide IRAnalyzer V1.9 software.

4.8. Other characterization techniques

Transmission Electron Microscopy (TEM) was performed with a JEOL-2100HT microscope, with a LaB_6 electron source, at a 200 kV operating voltage. The microscope was also equipped with a bottom mount Orius SC1000 CCD camera (Gatan). To prepare the NP samples for imaging, a carbon-coated 400 mesh copper grid from TED PELLA INC, underwent UV-ozone etching at 25°C for 30 minutes. Then 2 µL of NP dispersion, ranging in concentration between 0.03 and 0.06 mg/mL for LN and hybrid LN NPs, and 0.035 mg/mL for the pure AuSeeds dispersions, was dropped onto the grid and allowed to first air dry and then placed in an oven at 50°C for 10 minutes. All of the TEM images were treated with the ImageJ software. Energy-Dispersive X-Ray Spectroscopy (EDS) analysis was performed with the JEOL-2100HT microscope and with an EtTEM FEI TITAN both equipped with an EDX XMAX 80 mm^2 silicon drift detector for chemical maps. The EDS spectra were obtained using spot sizes of 35, 25 and 7 nm. Data were analysed by Aztec software (OXFORD INSTRUMENTS). The UV-visible absorption spectroscopy was performed with a SAFAS-UV mc2, double beam

spectrometer. The spectra acquisition was done by scanning the wavelengths from 400 to 1000 nm, using a bandwidth of 2 nm and a wavelength step of 1 nm. The samples were placed in a quartz cell with 1.0 cm path length. The Malvern nanoseries zetasizer ZS was used to obtain the hydrodynamic diameter and zeta potential of NP dispersions. NPs were dispersed in water at 25°C and concentrations were kept between 0.03 and 0.06 mg/mL for LN and hybrid LN NPs, and at 0.035 mg/mL for the pure AuSeeds dispersions. All measurements were done at 173° back-scattering angle with DTS1070 disposable folded capillary cells. Zeta potential data were fitted by the Smoluchowski model. The reported hydrodynamic diameters and zeta potential values were the average of triplicate measurements, and each measurement was the result of 30 runs. Error bars were the average of the standard deviations obtained from the three measurements. Inductive Coupled Plasma Atomic Emission Spectroscopy (ICP-AES) analysis was performed with an ICAP 6300 and an ICAP 6500 analysers by Thermofisher Scientific. The samples were digested in a solution containing 4% H_2SO_4, 4% HNO_3 and 4% HCl. HCl was used for samples containing gold.

Supporting Information

Supporting Information is available from the Wiley Online Library or from the author.

Acknowledgements

This work was supported by ANR in the frame of RACINE project (ANR-17-CE24-0029-03) and the 2015-2020 French Contrat Plan Etat Région (project E-TIME, SYMME). N. Blanchard and M. Bugnet from CLYM platform are thanked for their help with TEM experiments. T. Géhin and L. Berguiga are acknowledged for their implementation of the photothermal experiment set-up. XPS and ToF-SIMS data generated through access to the Nanobiotechnology Laboratory under the Framework of access to the Joint Research Centre Physical Research Infrastructures of the European Commission (BioActiveSurf).

References

[1] E. Hemmer, A. Benayas, F. Légaré, F. Vetrone, *Nanoscale Horizons* **2016**, *1*, 168.

[2] L. Cheng, C. Wang, L. Feng, K. Yang, Z. Liu, *Chem. Rev.* **2014**, *114*, 10869.

[3] Y. Liu, P. Bhattarai, Z. Dai, X. Chen, *Chem. Soc. Rev.* **2019**, *48*, 2053.

[4] L. R. Hirsch, A. M. bin, A. R. Lowery, F. Tam, R. A. Drezek, N. J. Halas, J. L. West, *Ann. Biomed. Eng.* **2006**, *34*, 15.

[5] J. A. Webb, R. Bardhan, *Nanoscale* **2014**, *6*, 2502.

[6] A. R. Rastinehad, H. Anastos, E. Wajswol, J. S. Winoker, J. P. Sfakianos, S. K. Doppalapudi, M. R. Carrick, C. J. Knauer, B. Taouli, S. C. Lewis, A. K. Tewari, J. A. Schwartz, S. E. Canfield, A. K. George, J. L. West, N. J. Halas, *Proc. Natl. Acad. Sci. U. S. A.* **2019**, *116*, 18590.

[7] C. Daoudi, M. O. Metidji, M. Remram, A.-M. Jurdyc, M. Martini, H. Gehan, D. Vouagner, *Eur. Phys. J. Appl. Phys.* **2018**, *82*, 20401.

[8] A. Plan Sangnier, R. Aufaure, S. Cheong, L. Motte, B. Palpant, R. D. Tilley, E. Guenin, C. Wilhelm, Y. Lalatonne, *Chem. Commun.* **2019**, *55*, 4055.

[9] S. J. Oldenburg, R. D. Averitt, S. L. Westcott, N. J. Halas, *Chem. Phys. Lett.* **1998**, *288*, 234.

[10] M. J. Garcia-Soto, O. Gonzalez-Ortega, *Gold Bull.* **2016**, *49*, 111.

[11] S. Wang, X. Zhao, J. Qian, S. He, *RSC Adv.* **2016**, *6*, 40615.

[12] J. Richter, A. Steinbrück, T. Pertsch, A. Tünnermann, R. Grange, *Plasmonics* **2012**, *8*, 115.

[13] Z. Xu, Y. Hou, S. Sun, *J. Am. Chem. Soc.* **2007**, *129*, 8698.

[14] D. K. Lee, Y. Song, V. T. Tran, J. Kim, E. Y. Park, J. Lee, *J. Colloid Interface Sci.* **2017**, *499*, 54.

[15] Y. Bao, K. M. Krishnan, *J. Magn. Magn. Mater.* **2005**, *293*, 15.

[16] M. Pita, J. M. Abad, C. Vaz-Dominguez, C. Briones, E. Mateo-Martí, J. A. Martin-Gago, M. Del Puerto Morales, V. M. Fernandez, *J. Coll. Interf. Sci.* **2008**, *321*, 484.

[17] D. Mott, J. Lee, N. Thi Bich Thuy, B. Thuy, Y. Aoki, P. Singh, S. Maenosono, *Jpn. J. Appl. Phys.*

2011, *50*, 065004.

[18] W. Shi, Y. Sahoo, M. T. Swihart, P. N. Prasad, *Langmuir* **2005**, 1610.

[19] R. Bardhan, N. K. Grady, T. Ali, N. J. Halas, *ACS Nano* **2010**, *4*, 6169.

[20] G. Campargue, L. La Volpe, G. Giardina, G. Gaulier, F. Lucarini, I. Gautschi, R. Le Dantec, D. Staedler, D. Diviani, Y. Mugnier, J. P. Wolf, L. Bonacina, *Nano Lett.* **2020**, *20*, 8725.

[21] D. Staedler, T. Magouroux, R. Hadji, C. Joulaud, J. Extermann, S. Schwung, S. Passemard, C. Kasparian, G. Clarke, M. Gerrmann, R. Le Dantec, Y. Mugnier, D. Rytz, D. Ciepielewski, C. Galez, S. Gerber-Lemaire, L. Juillerat-Jeanneret, L. Bonacina, J. P. Wolf, *ACS Nano* **2012**, *6*, 2542.

[22] J. Vuilleumier, G. Gaulier, R. De Matos, Y. Mugnier, G. Campargue, J.-P. Wolf, L. Bonacina, S. Gerber-Lemaire, *Helv. Chim. Acta* **2019**, *103*, e1900251.

[23] P. Zhao, N. Li, D. Astruc, *Zhao, P. Astruc, D.* **2013**, *257*, 638.

[24] R. Taitt, M. Urbain, Z. Behel, A.-M. Pablo-Sainz-Ezquerra, I. Kandybka, E. Millet, N. Martinez-Rodriguez, C. Yeromonahos, S. Beauquis, R. Le Dantec, Y. Mugnier, P.-F. Brevet, Y. Chevolot, V. Monnier, *Nanomaterials* **2021**, *11*, 950.

[25] M. Urbain, F. Riporto, S. Beauquis, V. Monnier, J. C. Marty, C. Galez, C. Durand, Y. Chevolot, R. Le Dantec, Y. Mugnier, *Nanomaterials* **2021**, *11*, 154.

[26] I. Y. Goon, L. M. H. Lai, M. Lim, P. Munroe, J. J. Gooding, R. Amal, *Chem. Mater.* **2009**, *21*, 673.

[27] K. E. Tettey, J. W. C. Ho, D. Lee, *J. Phys. Chem. C* **2011**, *115*, 6297.

[28] K. A. Whitaker, E. M. Furst, *Langmuir* **2014**, *30*, 584.

[29] N. T. K. Thanh, N. Maclean, S. Mahiddine, *Chem. Rev.* **2014**, *114*, 7610.

[30] K. A. Curtis, D. Miller, P. Millard, S. Basu, F. Horkay, P. L. Chandran, *PLoS One* **2016**, *11*, e0158147.

[31] S. K. Ghosh, T. Pal, *Chem. Rev.* **2007**, *107*, 4797.

[32] N. G. Bastus, J. Comenge, V. Puntes, *Langmuir* **2011**, *27*, 11098.

[33] L. Zhao, X. Ji, X. Sun, J. Li, W. Yang, X. Peng, *J. Phys. Chem. C* **2009**, *4*, 16645.

[34] H. Chen, L. Shao, Q. Li, J. Wang, *Chem. Soc. Rev.* **2013**, *42*, 2679.

[35] M. Grzelczak, J. Pérez-Juste, P. Mulvaney, L. M. Liz-Marzán, *Chem. Soc. Rev.* **2008**, *37*, 1783.

[36] W. Annan, P. Qing, L. Yadong, *Chem. Mater.* **2011**, *23*, 3217.

[37] Y. Xia, Y. Xiong, B. Lim, S. E. Skrabalak, *Angew. Chemie - Int. Ed.* **2009**, *48*, 60.

[38] G. F. Trindade, M. L. Abel, J. F. Watts, *Chemom. Intell. Lab. Syst.* **2018**, *182*, 180.

[39] A. Henderson, in *ToF-SIMS Mater. Anal. by Mass Spectrom.* (Eds.: J.C. Vickerman, D. Briggs), SurfaceSpectra Ltd And IM Publications LLP, **2013**, pp. 449–484.

[40] B. J. Tyler, G. Rayal, D. G. Castner, *Biomaterials* **2007**, *28*, 2412.

[41] D. J. Graham, D. G. Castner, *Biointerphases* **2012**, *7*, 49.

[42] J. Shlens, *arXiv:1404.1100* **2014**.

[43] Y. Pu, R. Grange, C. L. Hsieh, D. Psaltis, *Phys. Rev. Lett.* **2010**, *104*, 207402.

[44] K. Jiang, D. A. Smith, A. Pinchuk, *J. Phys. Chem. C* **2013**, *117*, 27073.

[45] J. R. Cole, N. A. Mirin, M. W. Knight, G. P. Goodrich, N. J. Halas, *J. Phys. Chem. C* **2009**, *113*, 12090.

[46] C. Bi, J. Chen, Y. Chen, Y. Song, A. Li, S. Li, Z. Mao, C. Gao, D. Wang, H. Möhwald, H. Xia, *Chem. Mater.* **2018**, *30*, 2709.

[47] A. Espinosa, J. Kolosnjaj-Tabi, A. Abou-Hassan, A. Plan Sangnier, A. Curcio, A. K. A. Silva, R. Di Corato, S. Neveu, T. Pellegrino, L. M. Liz-Marzán, C. Wilhelm, *Adv. Funct. Mater.* **2018**, *28*, 1803660.

[48] D. G. Duff, A. Baiker, P. P. Edwards, *Langmuir* **1993**, *9*, 2301.

[49] J. Riporto, M. Urbain, Y. Mugnier, V. Multian, F. Riporto, K. Bredillet, S. Beauquis, C. Galez, V. Monnier, Y. Chevolot, V. Gayvoronsky, L. Bonacina, R. Le Dantec, *Opt. Mater. Express* **2019**, *9*, 1955.

Received: ((will be filled in by the editorial staff))
Revised: ((will be filled in by the editorial staff))
Published online: ((will be filled in by the editorial staff))

Core-shell nanoparticles containing a lithium niobate core and a gold raspberry-shaped shell are prepared using a layer-by-layer protocol. The shell growth upon successive gold reduction steps is followed by several complementary characterization methods. Second Harmonic Generation is obtained due to the noncentrosymmetric structure of the core while the gold shell exhibits photothermia opening perspectives to use them as theranostic nanoprobes.

R. Taitt, M. Urbain, K. Brédillet, Z. Behel, G. Ceccone, J. Banuls-Ciscar, S. Beauquis, Y. Mugnier, P. F. Brevet, R. Le Dantec, Y. Chevolot, V. Monnier*

Gold raspberry shell grown onto non spherical lithium niobate nanoparticles for second harmonic generation and photothermal applications

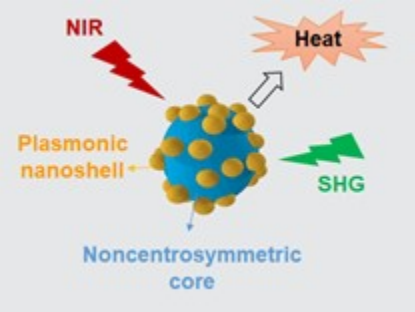

ToC figure